Construction of a new ternary α-MoO₃–WO₃/CdS solar nanophotocatalyst towards clean water and hydrogen production from artificial wastewater using optimal design methodology†

H. H. El-Maghrabi,[a] H. R. Ali[bc] and S. A. Younis*[bc]

Photocatalytic wastewater remediation and hydrogen generation were successfully achieved using a novel α-MoO$_{3(0.03)}$–WO$_{3(0.36)}$/CdS$_{(0.61)}$ heterojunction photocatalyst, fabricated by a solid-state approach. Through statistical optimal design of experiments (ODOE), simplex centroid design (SCD) and Box–Behnken design (BBD) were used to optimize the preparation and photocatalytic processes. The effects of combinatorial catalyst ratios on the photocatalytic responses were modeled using SCD under ultraviolet and visible light factors. Using BBD, the photodegradation experiments were fitted to the quadratic polynomial relationship with significance terms in the order of pH > catalyst dose > pollutants concentrations. The apparent first-order rate constants (K_{app}) of the developed ternary photocatalyst revealed that the solar-driven photoreaction is 1.4 times higher than the visible activation. The photocatalytic activities reached a maximum of 75% removal of total organic contaminants (TOC) and hydrogen yield of 8 μmol g^{-1} h^{-1} after 6 h of solar-harvesting with good photostability and durability for 5 cycles. The notable oxidation–reduction photoreaction of the ternary photocatalyst is attributed to the constructed Z-scheme by the synergic CdS–WO$_3$–α-MoO$_3$ heterojunction interaction. This work proves the power of ODOE to manufacture a photostable α-MoO$_{3(0.03)}$–WO$_{3(0.36)}$/CdS$_{(0.61)}$ solar-photocatalyst for a green environment.

1. Introduction

The exploration of pollution-free technologies for a clean environment is an urgent task, which has attracted extensive attention recently for sustainable human societies. Nanostructured semiconductor photocatalyst applications of far-reaching importance over the last decades include solar cells, water splitting, environmental remediation, self-cleaning, and so on.[1–3] Regarding water scarcity, water pollution is increasingly serious because of the indiscriminate discharge of untreated or partially treated wastewater into the ecosystem.[4] Therefore, constructing efficient treatment processes tackling water contamination is indispensable for facing the health crisis and water scarcity issues.[5,6]

Nowadays, one of the biggest challenges facing photoremediation applicability is the low stability and the fast recombination of photogenerated charges, resulting in partial wastewater treatment and second pollution.[5] As a promising approach, researchers have switched to heterostructural nanocomposite photocatalysts with compatible physicochemical and optical properties to promote photostability and charge carriers transfer.[7–10] By far, CdS nanowire has attracted intense attention in many fields, due to its unique band gap,[3,11] but the rapid electron–hole pairs recombination and photocorrosion of the CdS limit its practical applications in environmental remediation. To overcome CdS drawback, it should be stabilized with metal oxides exhibiting good optical and ion-transport properties, as well as stability in aqueous solutions. Among various nanostructured materials, molybdenum trioxide (MoO₃) and tungsten trioxide (WO₃) are well-known semiconductors with potential current applications in environmental and energy issues.[8,12] In fact, the unique crystallographic and anisotropic structures of MoO₃ and WO₃ [7,9,13] give us an inspiration that CdS can couple with MoO₃ and WO₃ semiconductors to form heterojunction nanocomposites. This structure can provide a novel heterojuncted photocatalyst with energetically matching band–band phenomenon, which seem a promising photostable material relevant to the target applications in clean water and hydrogen production using solar energy. To the best of our knowledge, there is no research about the synthetic strategy for such ternary photocatalyst till now. Therefore, the

ᵃCatalysis Division, Petroleum Refining Department, Egyptian Petroleum Research Institute, 11727 Nasr City, Cairo, Egypt

ᵇSpectroscopic Division, Analysis and Evaluation Department, Egyptian Petroleum Research Institute, 11727 Nasr City, Cairo, Egypt. E-mail: sherifali_r@yahoo.com; sherifali@epri.sci.eg; Tel: +20 1 228877458

ᶜLiquid Chromatography Unit, Central Laboratories, Egyptian Petroleum Research Institute, 11727 Nasr City, Cairo, Egypt

† Electronic supplementary information (ESI) available. See DOI: 10.1039/c6ra25146c

combinatorial rational design is an effective strategy for the development of a novel heterostructural composite consisting of CdS, α-MoO$_3$ and WO$_3$ nanomaterials for solar-harvesting.

In the present study, simplex centroid design (SCD) was used to investigate and optimize the combinatorial ratios of α-MoO$_3$, WO$_3$ and CdS catalysts to fabricate photostable solar-harvester nanocomposite. Following that, Box–Behnken design (BBD) was used to study the effect of operational variables on the photocatalytic performance using the fabricated nano-composite in synthetic wastewater containing benzoic acid as a model pollutant. Expression mathematical models between the semiconductor combinatorial ratios as well as the opera-tional variables and photo-remediation efficiencies were simu-lated and statistically validated. Furthermore, potential application of the developed α-MoO$_3$–WO$_3$/CdS nanocomposite to promote utilization of solar light for practical wastewater decontamination and hydrogen energy generation were inves-tigated. A possible photocatalytic mechanism on the basis of experimental and optical results was also presented. Herein, the detailed examination will provide the fundamental approach to design efficient photostable photocatalysts as solar clean tech-nology for a green production of clean water and hydrogen energy.

2. Experimental

2.1. Synthesis of α-MoO$_3$–WO$_3$/CdS ternary photocatalyst

In the first stage, CdS hexagonal phase was prepared from Cd(NO$_3$)$_2$4H$_2$O and NH$_2$CSNH$_2$ precursors in a Teflon-lined stainless steel autoclave;[14,15] whilst the WO$_3$ and α-MoO$_3$ pha-ses were prepared from their ammonium salts by the modified Pechini method.[16,17] In the second stage, the α-MoO$_3$–WO$_3$/CdS binary and ternary nanocomposites were prepared by one-step physical solid-state method in a planetary mill using 18 mm stainless steel balls. Typically, the combined photocatalyst with the desired SCD ratios in Table (S1)† were accurately weighted and mixed together. The mixed catalyst was then grounded continuously in the planetary mill for 180 minutes to assure an entire reaction. After that, the stainless-steel balls were cleaned in order to recover the loaded catalysts. The nanocomposite obtained was washed with ethanol, then dried at 378 K for 2 h and labeled as MoO$_{3x}$–WO$_{3y}$/CdS$_{(1-x+y)}$, where x and y are the ratios of catalysts and equal 0, 0.17, 0.33, 0.50, 0.67, and 1 (Table S1†). For comparison, the pure α-MoO$_3$, WO$_3$, and CdS catalysts were grounded separately under the same conditions.

The typical synthetic procedures and the experimental characterization instruments for HR-TEM, EDS, PXRD, FTIR, Raman, BET surface area, the UV-vis diffuse reflectance and photoluminescence (PL) properties are present in the ESI.†

2.2. Development of ODOE experiment for photocatalytic optimization

ODOE is a systematic methodology devoted to the evaluation of relationships existing between a cluster of experimental vari-ables and response results according to one or more targeted criteria and controlling them toward optimization.[18] In the present case, the response target was to develop stable ternary photocatalyst as solar-harvester. If all studied variables are assumed significant, the response results can be expressed as (eqn (1)) with the aim being to optimize the Y response.

$$Y = \int (X_1, X_2, \ldots, X_k) \tag{1}$$

To develop an appropriate model of approximation to express the actual relationship between processes' variables and the responses, it is supposed that the studied variables are continuous and controllable by experimental design. Therefore, second order quadratic polynomial (eqn (2)) is considered a full model in ODOE experiments.

$$Y\% = \beta_o + \sum_{i=1}^{k} \beta_i X_i + \sum_{i=1}^{k} \sum_{i=1,i<j}^{k} \beta_{ij} X_i X_j + \sum_{i=1}^{k} \beta_{ij} X_i^2 + \varepsilon \tag{2}$$

where $Y\%$ refers to the predicted response, β_o is the constant coefficient, x_i and x_j are the studied variables, k is the number of variables, β_i, β_{ii} and β_{ij} are the model coefficients terms, and ε is the deviation error (negligible).

In this work, two classes of ODOE methodologies including combinatorial and factorial design were applied for multivar-iate optimization of the synthetic and application variables. First, SCD design was used to evaluate and maximize the combinatorial ratios of CdS (A), WO$_3$ (B) and α-MoO$_3$ (C) considering photodegradation of benzoic acid, a model pollutant, as response criteria under ultraviolet and visible light factors (Table S1†). A total of 20 SCD points divided to 10 augmented runs ($10 = k^2 + 1$; $k = 3$) divided as 3 single, 3 binary and 4 ternary catalysts at each light factor and considering the ratios of $A + B + C = 1$ (Fig. S1a†). Based on SCD design, poly-nomial modeling (eqn (3)) with no intercept was best selected to represent the mathematical relation between the photo-degradation activities and the combinatorial ratios under both lights sources.

$$Y\% = \beta_1 A + \beta_2 B + \beta_3 C + \beta_{12} AB + \beta_{13} AC + \beta_{23} BC + \beta_{123} ABC \tag{3}$$

Second, 17 rotatable BBD matrix ($17 = k^2 + k + c_p$; $k = 3$ and $c_p = 5$ central points) was adopted to test and optimize the photodegradation rate by ternary photocatalyst developed by SCD above using visible activation. In this stage, BBD was designated to evaluate the influences of the operational vari-ables on the photodegradation responses to avoid unacceptable results that might occur. For this procedure, the three inde-pendent variables including the photocatalyst dose ($X_1 = 0.5$–1.5 g l^{-1}), initial concentrations ($X_2 = 50$–150 mg l^{-1}), and pH ($X_3 = 4$–10) on the photodegradation response were investigated (Table S2 and Fig. S1b†). Using BBD, the experimental results were found fitted to an empirical quadratic polynomial model eqn (4) at the studied constraints levels.

$$Y\% = \beta_o + \beta_1 X_1 + \beta_2 X_2 + \beta_3 X_3 + \beta_{12} X_1 X_2 + \beta_{13} X_1 X_3 + \beta_{23} X_2 X_3 + \beta_{11} X_1^2 + \beta_{22} X_2^2 + \beta_{33} X_3^2 \tag{4}$$

For ODOE experimental setup, Design-Expert® (v. 7.0.1) and MINITAB (v. 17) statistical software package were utilized to design the experiments matrix. After each photocatalytic experiment, the photodegradation efficiencies were quantified by a high-performance liquid chromatography equipped with diode array detector (HPLC-DAD) instrument. The details of photocatalytic experiments and analytical procedures are presented in the ESI.†

2.3. Statistical validation

The statistical computational analysis of the combinatorial and experimental variables and their interactions on the responses data were tested by the analysis of variance (ANOVA) at probability (p) level of 0.05 and response surface diagrams. ANOVA statistics results were assessed with Student's (t-ratio), percentage of contribution $\left(PC\% = \dfrac{SS}{\sum SS} \times 100 \right)$, determination coefficient (R^2) and standard error of prediction (RSEP, eqn (5)) descriptive values. The statistics results were used to further evaluate the goodness of the simulated model fitting and the statistical relation of the model component levels on response results.

$$RSEP = \sqrt{\frac{\sum\limits_{i=1}^{N} \left(Y_{pred,i} - Y_{exp,i} \right)^2}{\sum\limits_{i=1}^{N} \left(Y_{exp,i} \right)^2}} \times 100 \qquad (5)$$

where $Y_{pred,i}$ and $Y_{exp,i}$ are the predicted and experimental response values, and N is the number of experiments.

3. Results and discussion

The development of heterojunction ternary photocatalysts is an effective procedure to promote the photocatalytic performance of semiconductors. In this research, optimization strategies aim not only to find out the highest photocatalytic rate, but also to provide best possible numerical ratios to fabricate a photostable nanocomposite with broad wavelengths responses for subsequent economical reuse in aqueous environment. To achieve these goals, the parallel synthesis and application strategies of single, binary and ternary photocatalysts guided by statistical ODOE approach through SCD and BBD methodologies are used for optimization.

3.1. Development of α-MoO$_{3(0.03)}$–WO$_{3(0.36)}$/CdS$_{(0.61)}$ nanocomposite using ODOE approach

From the combinatorial SCD response results given in Table (S1),† it is seen that the ultraviolet-activation exhibit adequately higher photodegradation (8.7–78.5%) compared to visible-activation (5.4–69.8%). Following the SCD design, two numerical polynomial equations were developed for the benzoic acid photodegradation in terms of the photocatalysts ratios as factor of light type as seen in eqn (6) and (7).

$$Y_{uv} = 0.44A + 0.45B + 0.07C + 0.014AB + 4.88AC - 7.17BC - 1.05ABC \qquad (6)$$

$$Y_{vis} = 0.38A + 0.26B + 0.04C + 0.015 - AB - 2.31AC - 3.17BC - 1.12ABC \qquad (7)$$

where Y_{uv} and Y_{vis} represent photodegradation% at ultraviolet and visible light, respectively.

Validation statistics in Table 1 reveal that the two equations (eqn 6 and 7) are highly significant with F_{model} 507.04 at $p < 0.0001$ and high R^2 (R_{pred}^2 0.976 and R_{adj}^2 0.995) and Adeq precision of 79.53. Low RSEP statistic, indicating the best model structures to predict the responses data with 1.28% to 1.49% chance of lack of fit could occur due to noise. Experiment *versus* predicted photodegradation plot of the model results are distributed symmetrically on a 45° line (Fig. S2†). This provides further confirmation of a precise model hypothesis to represent the photodegradation responses under the given photodegradation domain at the design space.

Graphical 3D plots in Fig. 1a show that CdS ratio has the highest synergetic effect on visible-activation response; whilst a higher α-MoO$_3$ content could lead to the decrease of visible-activation rate. This finding is in accordance with the statistical results in Table 1 and their related literature data.[19,20] Additionally, it is remarkable that the photo-illumination response of binary and ternary nanocomposites has the lowest light dependent with PC% of 1.35% and 0.06% comparable to single catalysts with PC% 7.05% (Table 1). Among nanocomposites, the ternary α-MoO$_3$–WO$_3$/CdS combinations "ABCD" showed the lowest photocatalytic difference relevant to light types (p-value 0.025–0.096) with paired t-test of 5.79 at 95% confidence. These results indicated that the ternary photocatalysts could have broad wavelengths activation responses. Based on the SCD design data, numerical optimization of ternary photocatalyst was carried out using the statistical and experimental approach. The

Table 1 ANOVA statistical results of the simulated SCD combinatorial models under both ultraviolet and visible lights effects

| Terms	DF	SS	MS	F-Value	Prob > F	PC%
Regression model	13	8385.72	645.06	507.04	<0.0001	—
Linear model	2	5386.6	822.25	646.31	0.0001	64.18
Quadratic model	3	2281.39	734.72	577.51	0.0001	27.18
AB	1	1930.44	1694.33	1331.8	<0.0001	23.00
AC	1	39.74	45.61	35.85	0.001	0.47
BC	1	311.21	225.62	177.34	0.0001	3.71
ABC	1	17.22	17.22	15.68	0.025	0.21
Light effect						
Linear model	3	592.00	76.54	60.16	<0.0001	7.05
AD	1	310.95	19.33	15.2	0.008	3.70
BD	1	252.48	209.67	164.81	0.001	3.01
CD	1	28.57	6.13	4.82	0.071	0.34
Quadratic model	3	113.57	37.04	29.12	0.001	1.35
ABD	1	1.09	3.38	2.66	0.154	0.01
ACD	1	83.72	55.1	43.31	0.001	1.00
BCD	1	28.76	33.68	26.47	0.002	0.34
$ABCD$	1	4.94	4.94	3.89	0.096	0.06
Residual error	6	7.63	1.27			0.09
Total	19	8393.35				
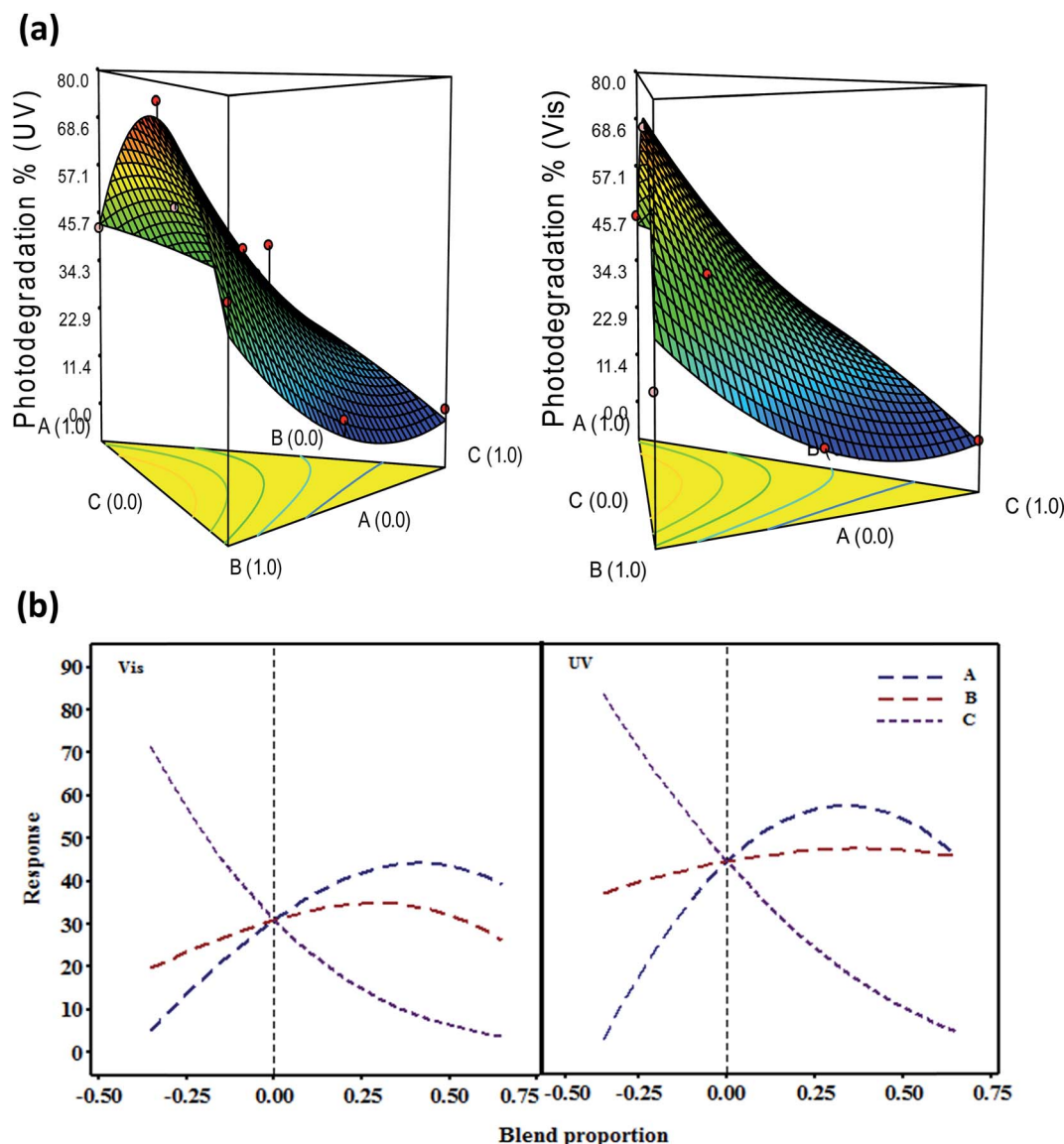
Fig. 1 (a) Ternary contour plots and (b) Cox response trace plots of the effects of catalysts ratios on benzoic acid photodegradation rates under visible and ultraviolet lights.

optimum desirable stoichiometric ratios of 0.61 : 0.36 : 0.03 wt% for CdS, WO$_3$, and α-MoO$_3$ is simulated to build a photostable nanocomposite photocatalyst with maximum photodegradation percentage under the design constraints. The combinatorial ratios obtained confirmed by Cox trace plot (Fig. 1b), which shows the stoichiometric effects of catalysts ratios on the response values. Under these combination proportion, the predicted and experimental benzoic acid removal rates were respectively 70.54% and 73.8% under ultraviolet light, and 64.67% and 65.28% under visible light. In addition, it was found that this fabricated ternary photocatalyst possessed an extended solar harvesting response toward benzoic acid removal with about 70.63% photodegradation rate. This enhanced photocatalytic performance under direct solar irradiation is the reason that α-MoO$_{3(0.03)}$−

WO$_{3(0.36)}$/CdS$_{(0.61)}$ photocatalyst developed herein is selected for continuous characterization.

3.2. Characterization

3.2.1. Mineralogical and morphological analysis. Fig. 2a shows the PXRD properties of the fabricated catalysts. The PXRD diffraction peaks for single catalysts are in good agreement with diffraction indexed to a hexagonal phase for both CdS (PCPDF WIN: 751545)[15] and WO$_3$ (JCPDS: 75-2187)[21] and orthorhombic phase for MoO$_3$ (JCPD: 35-0609) as discussed in the ESI.[22,23]† For α-MoO$_{3(0.03)}$−WO$_{3(0.36)}$/CdS$_{(0.61)}$ ternary nanocomposite, the PXRD shows all CdS patterns besides week diffraction indexed to WO$_3$ ($2\theta = 23.13°$, $24.13°$ and $24.48°$) and α-MoO$_3$ ($2\theta = 12.8°$, $23.13°$, $25.81°$ and $39.48°$) phases. Raman spectra in Fig. 2b confirmed the well fabrication of the ternary α-MoO$_{3(0.03)}$−WO$_{3(0.36)}$/CdS$_{(0.61)}$ photocatalyst. The

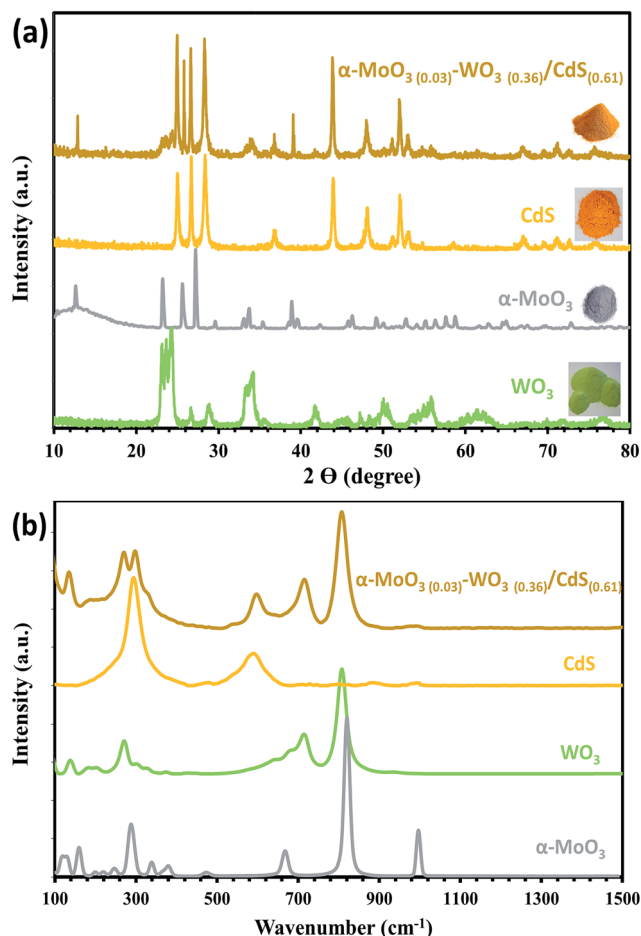**Fig. 2** (a) PXRD and (b) Raman patterns of α-MoO$_3$, WO$_3$, CdS, and the α-MoO$_{3(0.03)}$–WO$_{3(0.36)}$/CdS$_{(0.61)}$ nanostructure photocatalysts.

Raman and FTIR peak shifted is due to the increase or decrease in the vibration constant of the developed hybrid ternary photocatalytic system.

The epitome FESEM image in Fig. 3a shows that CdS appears as nanowires with the rod-like geometry containing a uniform distribution of α-MoO$_3$ and WO$_3$ nanoparticles along the surface. Such a smooth compact layer of α-MoO$_{3(0.03)}$–WO$_{3(0.36)}$/CdS$_{(0.61)}$ was confirmed by HRTEM (Fig. S4†) that showed typical wrinkles and folds of the CdS sheets having un-agglomerated WO$_3$ and α-MoO$_3$ spherical nanoparticles (30–50 nm) on the surface. The geometry of CdS has a width of 200–300 nm to several micrometers in length. From the energy dispersive X-ray spectrum, EDS, in Fig. 3b, it can be unambiguously shown that the α-MoO$_{3(0.03)}$–WO$_{3(0.36)}$/CdS$_{(0.61)}$ contains only the signals of O, S, Cd, W and Mo with ratios of 8.45, 13.55, 47.6, 28.6, and 1.98, respectively, which is very close to the stoichiometric ratio of the fabricated ternary system. Also, a hierarchical of the nanocomposite structure observed by EDS is beneficial to promoted electron–hole pair's transfer and separation due to the intimate interfaces interaction resulting in forming the heterojunction between CdS and α-MoO$_3$, and WO$_3$. Furthermore, the selected area electron diffraction (SAED) pattern in Fig. 3c revealed that the developed α-MoO$_{3(0.03)}$–WO$_{3(0.36)}$/CdS$_{(0.61)}$ ternary photocatalyst is a polycrystalline, which has a single-phase crystal with the (110) growth direction. Particularly, the interplanar fringes of d = 0.35 nm and 0.20 nm on CdS nanowire (Fig. 3d) correspond to the (002) and (110)
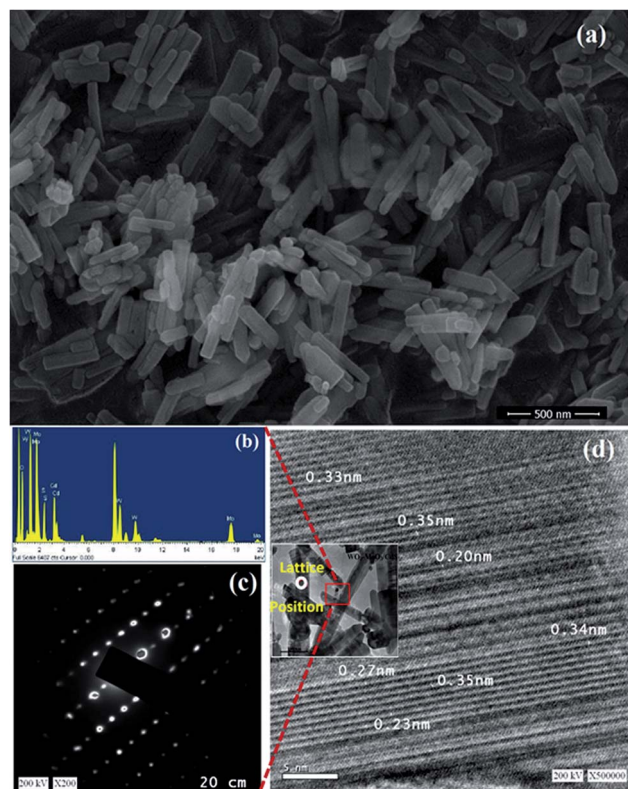

Fig. 3 (a) FESEM image, (b) EDS spectrum, (c) SAED pattern and (d) lattice HRTEM of α-MoO$_{3(0.03)}$–WO$_{3(0.36)}$/CdS$_{(0.61)}$ ternary photocatalyst.

disappearance of the low-frequency Raman peaks of α-MoO$_3$ at 197, 217, 244, 287, 364, 378, 470, 666, and 990 cm^{-1} is due to its low combinatorial ratio (3%) in the ternary nanocomposite. The α-MoO$_3$ Raman peaks at 666 cm^{-1} and 990 cm^{-1} were specified to the Mo$_3$–O of triply coordinated bridge-oxygen and Mo=O asymmetric stretching modes of terminal (unshared) oxygen. The intense peaks at 302 and 603 cm^{-1} are assigned to the first (1LO), and the second (2LO) order longitudinal optical phonon of CdS.[24] Low Raman frequencies at 130 cm^{-1} and 180 cm^{-1} are attributed to (W$_2$O$_2$)$_n$ chains of WO$_3$. The high-frequency at 806 cm^{-1} correspond to the W–O–W stretching of WO$_3$ network[25] and red shifted Mo$_2$–O stretching of doubly coordinated oxygen in α-MoO$_3$.[23] The negative shift of the Mo$_2$–O stretching mode caused by corner-shared oxygen atoms in common to two MoO$_6$ octahedrons from 813 cm^{-1} to 806 cm^{-1} is due to the decrease in the vibration constant of the ternary system. In addition, the features at 273 cm^{-1} is also assigned to W–O–W bending of bridging oxide[26] and O=Mo=O wagging mode that shifted from 287 cm^{-1} position at pure α-MoO$_3$. Moreover, the FTIR peaks of α-MoO$_{3(0.03)}$–WO$_{3(0.36)}$/CdS$_{(0.61)}$ ternary photocatalyst spotted all the vibration modes assigned between α-MoO$_3$, WO$_3$ and CdS bonds in the ternary nanocomposite (Fig. S3†). The noted

lattice faces of wurtzite CdS, respectively. Moreover, BET isotherms of the developed single and ternary photocatalysts (Fig. S5a†) possess a stepwise adsorption and desorption hysteresis, IUPAC Type IV isotherms, with the characteristics of a mesoporous surface.[27] The detailed BET data are listed in Table S3.† The BET isotherms indicated that the developed ternary photocatalyst may possess a hollow core or cavity caused by the packing of three nanomaterials as demonstrated by increased pore volume with a high peak apex at about 12 nm (Fig. S5b).† Compared with pure catalysts, the α-MoO$_{3(0.03)}$–WO$_{3(0.36)}$/CdS$_{(0.61)}$ ternary photocatalyst exhibits more distinctive BET properties. It can be due to the small capillary condensation step in the fabricated heterojuncted structure appeared in the range of 0.8–1.0 P/P_o with a hollow core or cavity, as demonstrated by increased pore volume peak apex at about 12 nm (Fig. S5b).† For photocatalytic reactions, an increase of surface area provided more active sites not only to anchor organic pollutants from aqueous solution for photodegradation, but also make charge carriers transport easier from the interior to surface to react with adsorbed water and hydroxyl groups to form oxidative radicals.[28,29] So, the photocatalytic performance will dramatically increase with the obtained high surface area of nanocomposite material. Overall characteristic results indicate that the crystallinity and

structural integrity of 1D CdS nanowires are not degraded by 3D α-MoO$_3$ and WO$_3$ nanoparticles incorporation.

3.2.2. Optical analysis. Fig. 4a represented the UV-visible diffuse reflection spectra (UV-vis DRS) of the as-prepared single and ternary photocatalysts. In comparison to single catalysts, the absorption intensity of the developed ternary photocatalyst slightly enhanced to exhibit a high broadband visible light absorption edge at 508 nm with a narrow band gap (E_g = 2.33 eV) lower than pure catalysts by 0.09 to 0.72 eV (entire set Fig. 4a) (ESI†). The lower band gap energy of the α-MoO$_{3(0.03)}$–WO$_{3(0.36)}$/CdS$_{(0.61)}$ nanocomposite probably ascribes to the formed interband edges in the nanocrystals. Where, α-MoO$_3$ and WO$_3$ can distort the CdS band structure particularly through expansion of the van der Waals gap, and discrete electronic interband states (CB) of their own close to the CB edge, between the VB and CB, of CdS, which consequently improving the flow of electrons transfer.[19,30–32] Thus, the new developed band edges can effectively modulate and decrease band gap structure of the synthesized ternary nanocomposite material as described herein after (*cf.* Section 3.5.). This obtained narrow band gap of the α-MoO$_{3(0.03)}$–WO$_{3(0.36)}$/CdS$_{(0.61)}$ nanocomposite not only promotes the absorption of more photons in sunlight, but also enhances the excitation of photogenerated electrons in visible region and increases
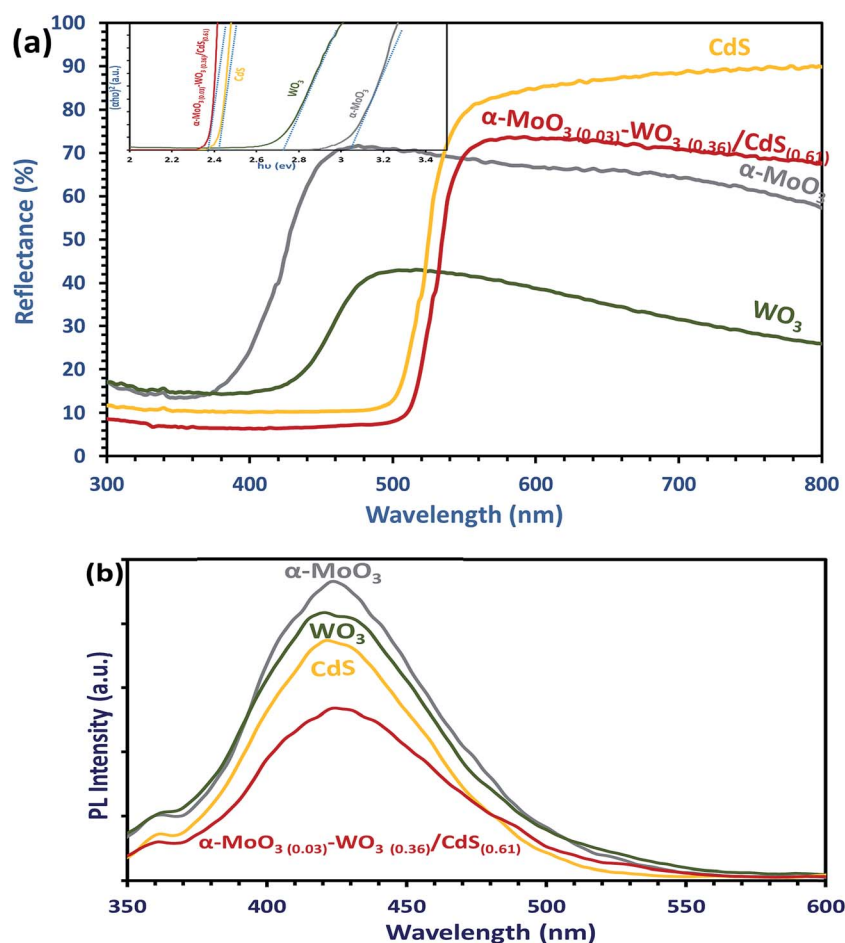

Fig. 4   (a) UV-vis DRS and (b) PL optical properties of the developed nanostructure catalysts.

photocatalytic performances towards photodegradation and H_2 production activities. Furthermore, as seen from PL spectra (Fig. 4b), all the catalysts exhibit approximately similar PL spectra with strong emission broad band range between 390 and 520 nm centering at about 425 nm, attributing the energy band–band PL phenomenon. Obviously, the α-MoO$_{3(0.03)}$–WO$_{3(0.36)}$/CdS$_{(0.61)}$ ternary photocatalyst showed the lowest recombination rate of the photogenerated carriers. The enhanced PL properties may arise from the heterojunction structure and the yielded vacancies associated with CdS ratio due to the smaller radius of S^{2-} than that of Cd^{2+}, W^{3+} and Mo^{3+}.[19,20,33] This indicates that the developed red-shifted light of α-MoO$_{3(0.03)}$–WO$_{3(0.36)}$/CdS$_{(0.61)}$ can be ascribed to the modification by CdS photocatalyst, which efficiently promotes the electrons–holes separation by the strong intimate interfaces interaction between CdS and WO$_3$, and α-MoO$_3$ in the ternary

photocatalyst. Based on the data above, it can be suggested that the developed α-MoO$_{3(0.03)}$–WO$_{3(0.36)}$/CdS$_{(0.61)}$ heterojuncted photocatalyst could have high photocatalytic activities under broad wavelengths as further studied hereinafter.

3.3. Evaluation and optimization of α-MoO$_{3(0.03)}$–WO$_{3(0.36)}$/CdS$_{(0.61)}$ photodegradation activity

3.3.1. BBD regression modeling. Referring to the BBD experimental responses (Table 2), a numerical mathematical equation (eqn (8)) was developed to simulate benzoic acid photodegradation rate by α-MoO$_{3(0.03)}$–WO$_{3(0.36)}$/CdS$_{(0.61)}$ under three variables conditions and visible-activation.

$$Y_{photo-vis\%} = +44.21 + 9.43X_1 - 8.47X_2 - 22.78X_3 - 5.17X_1X_2 - 3.95X_1X_3 + 0.68X_2X_3 + 0.84X_1^2 + 3.08X_2^2 + 7.22X_3^2 \quad (8)$$

From the resultant responses in Table 2, a wide variation in the BBD responses from 23.4% to 88.5% were observed, indicating that the photodegradation was efficiently affected by the selected variables. This is also notable by the wide range of coefficients values in eqn (8). At 95% confidence, the suitability of numerical quadratic model (eqn (8)) is confirmed by regression statistical results in Table (S4)† and the correlation curve in (Fig. S2b†). As it is evident, the statistical data confirm reasonably well-behaved quadratic equation to represent the photoresponses with an excellent linear regression fit ($R^2 = 0.9993$) to the experimental results.

3.3.2. Estimation of interactive effect of experimental variables. The quantitative effects of the operational variables on the benzoic acid photodegradation responses using the α-MoO$_{3(0.03)}$–WO$_{3(0.36)}$/CdS$_{(0.61)}$ photocatalyst were determined using ANOVA tools in Table 3. From ANOVA, the significant effect of the experimental components can be ranked as linear (X_i, PC% 92.31%) > quadratic (X_i^2, PC% 4.73%) > interaction (X_iX_j, PC% 2.91%) effects (Table 3). Among all variables, the pH variable, X_3, ($t = -90.29$ and $F = 8152.01$) and its quadratic term, X_3^2, ($t = 20.75$ and $F = 430.65$) have the highest significant

Table 2 Three-variables Box–Behnken design (BBD) matrix as a function of the benzoic acid photodegradation response (%) by α-MoO$_{3(0.03)}$–WO$_{3(0.36)}$/CdS$_{(0.61)}$ under visible light

Std	Run	X_1	X_2	X_3	Photodegradation%			
					Experimental	Predicted	Residual	Error%
3	1	−1	1	0	36.0	35.4	0.6	1.77
2	2	1	−1	0	70.6	71.2	−0.6	−0.90
16	3	0	0	0	44.2	44.2	0.0	0.07
8	4	1	0	1	35.9	35.0	0.9	2.53
5	5	−1	0	−1	60.8	61.7	−0.9	−1.50
13	6	0	0	0	44.0	44.2	−0.2	−0.52
15	7	0	0	0	44.2	44.2	0.0	0.03
4	8	1	1	0	43.5	43.9	−0.4	−0.86
12	9	0	1	1	23.4	23.9	−0.5	−2.29
9	10	0	−1	−1	87.0	86.4	0.5	0.62
10	11	0	1	−1	68.4	68.1	0.3	0.40
11	12	0	−1	1	39.2	39.5	−0.3	−0.69
1	13	−1	−1	0	42.4	42.0	0.4	0.88
7	14	−1	0	1	23.9	24.0	−0.1	−0.42
6	15	1	0	−1	88.5	88.4	0.1	0.11
14	16	0	0	0	44.2	44.2	0.0	0.03
17	17	0	0	0	44.4	44.2	0.2	0.39

Table 3 ANOVA results of the BBD model for the prediction of benzoic acid photodegradation efficiency

Terms	DF	Effect	SS	Standard error	t-Value	F-Value	Prob > F	PC%
Constant	9	—	5885.38	0.32	138.53	1284.25	<0.0001	—
X_1	1	18.86	711.73	0.25	37.39	1397.75	<0.0001	12.09
X_2	1	−16.93	573.36	0.25	−33.56	1126.02	<0.0001	9.74
X_3	1	−45.56	4150.94	0.25	−90.29	8152.01	<0.0001	70.49
X_1X_2	1	−10.35	107.03	0.36	−14.5	210.19	<0.0001	1.82
X_1X_3	1	−7.89	62.25	0.36	−11.06	122.26	<0.0001	1.06
X_2X_3	1	1.35	1.83	0.36	1.89	3.59	0.1001	0.03
X_1^2	1	1.68	8.42	0.35	2.41	5.81	0.0467	0.14
X_2^2	1	6.16	50.53	0.35	8.86	78.43	<0.0001	0.86
X_3^2	1	14.43	219.29		20.75	430.65	<0.0001	3.73
Residual	7		3.56					
Lack-of-fit	3		3.48			56.01	0.0010	
Pure error	4		0.08					
Total	16		5888.94					

influences on photo-response at p-level < 0.0001. ANOVA statistics were further confirmed by both the Pareto and contribution charts shown in (Fig. S6).†

The response surface diagrams to understanding the linear and interaction variables effects on α-MoO$_{3(0.03)}$–WO$_{3(0.36)}$/CdS$_{(0.61)}$ photo-response are presented in Fig. 5. A perturbation plot in Fig. 5a shows high linear curvatures of first-order lines
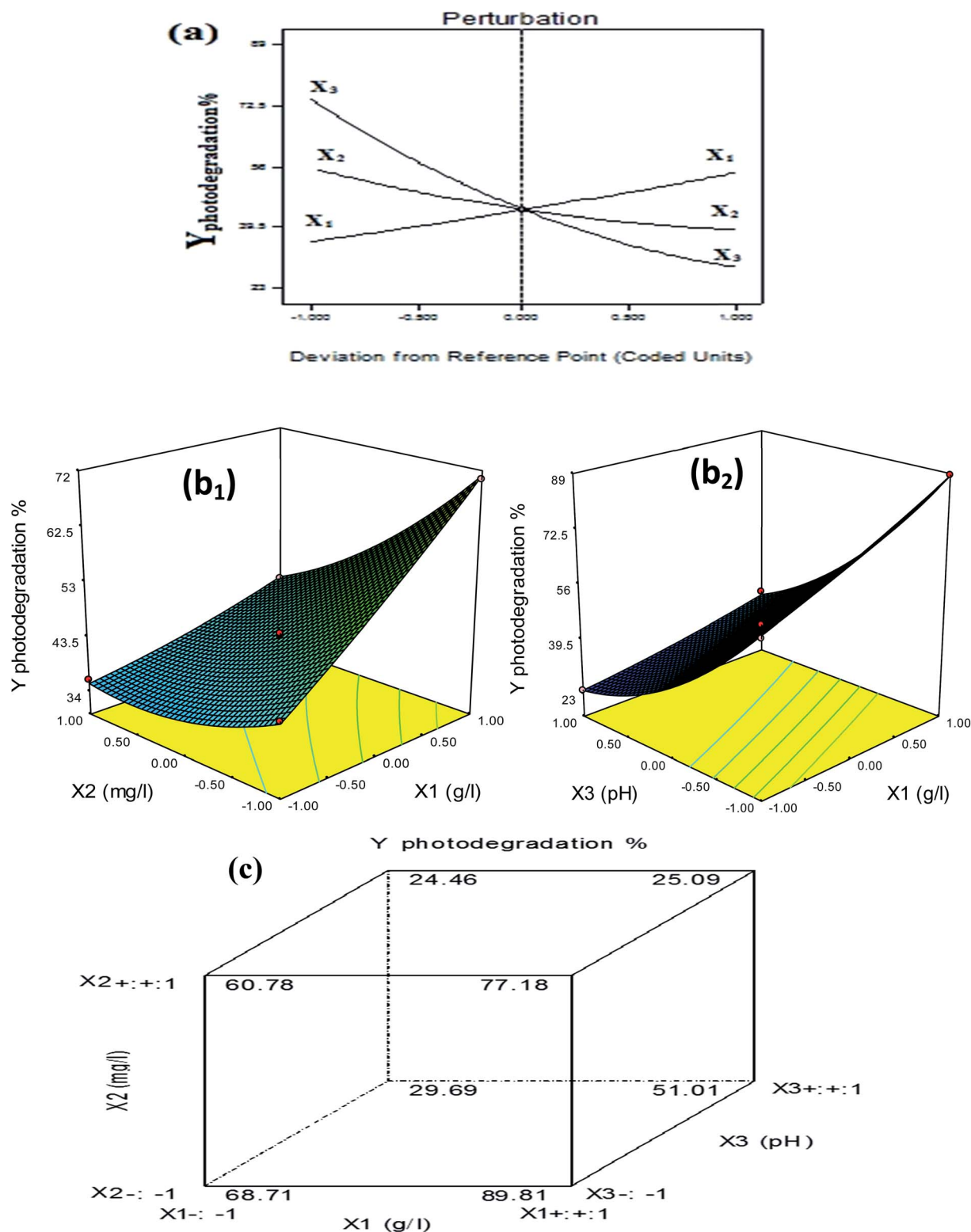

Fig. 5 Graphical diagrams of (a) the linear perturbation plots, (b) 3D surface contour plots, and (c) the cubic plots for benzoic photodegradation using α-MoO$_{3(0.03)}$−WO$_{3(0.36)}$/CdS$_{(0.61)}$ as a function of visible light.

with change levels along the design space. The 3D plots in Fig. 5b_1 showed a raising trend in photodegradation performance at high catalyst dose and low benzoic concentration levels. This may be due to an increase in the free available reactive site species at a higher photocatalyst dose, resulting in enhancement of the migration of electron–hole pairs. While, at high benzoic concentrations, the illumination light is diminished to reach the photocatalyst surface of major fraction due to the increase of equilibrium adsorption and increase of the depth of bulk aqueous (higher turbidity) penetration. The 3D plot for X_1X_3 in Fig. 5b_2 showed that the photodegradation rate is sharply decreased in alkaline pH with minor interactions with catalyst dose. At alkaline pH, the adsorbed amount of benzoic acid on the catalyst surface decreased due to increases of ion-dipole repulsion between the negatively charged ^-OH anions adsorbed on the surface and the negative pole of the benzoate (COO^-) at pH > pK_a (4.2). At this point, the likely adsorbed ^-OH ions is suggested to consume the electron–holes on the excited catalyst surface and generate $^\cdot OH$ radicals rather than photodegradation of dissolved benzoate anions in solution.

Moreover, the simultaneous cube plot response of the operational variables in Fig. 5c demonstrated that the α-$MoO_{3(0.03)}$–$WO_{3(0.36)}$/$CdS_{(0.61)}$ photo-response is highly dependent on the selected variables at a particular point in the design constraints. Notably, the sharp increase in photodegradation% was seen with an increase X_1 from 68.71% (coded −1) to 89.81% (coded +1). Whereas, the gradual decrease in photodegradation% was seen with increase X_2 from 68.71% (coded −1) to 60.78% (coded +1) and X_3 from 89.81% (coded −1) to 51.01% (coded +1).

3.3.3. Optimization conditions and model validation.

Based on the BBD data above, quantitative optimization of benzoic acid photodegradation by α-$MoO_{3(0.03)}$–$WO_{3(0.36)}$/$CdS_{(0.61)}$ was carried out under visible activation factor. Accordingly, at 100 mg l^{-1} benzoic acid, the numerical optimum values are presented as 1.42 g l^{-1} photocatalyst dose and 4.86 pH with predicted 80.22% photodegradation rate. To check the validity of the simulated model, the experimental photodegradation response of 81.38% ± 0.45 was obtained under the same optimum conditions, which is in agreement with that of the predicted response. Therefore, the developed
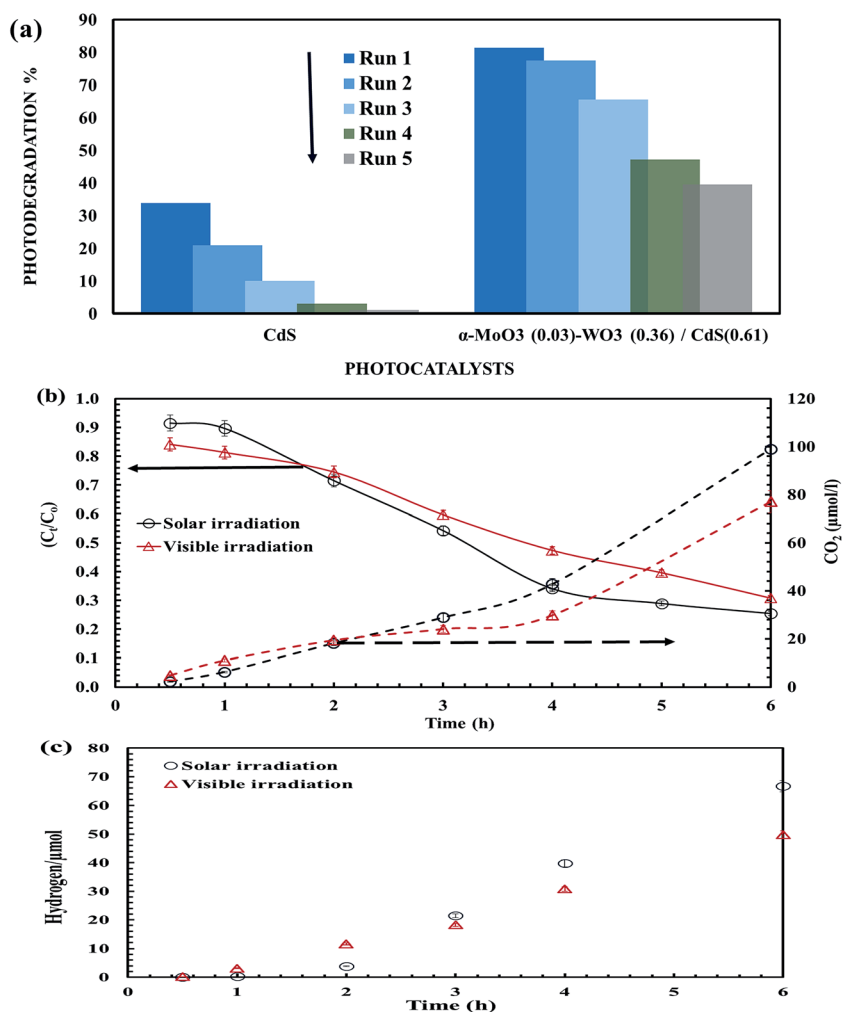

Fig. 6   (a) Photostability, (b) TOC photo-reduction, and (c) H_2 generation using α-$MoO_{3(0.03)}$–$WO_{3(0.36)}$/$CdS_{(0.61)}$ heterojunction photocatalyst under visible and solar lights.

mathematical equation (eqn (8)) was experimentally and statistically considered in this work to predict the benzoic acid photodegradation by α-$MoO_{3(0.03)}$–$WO_{3(0.36)}$/$CdS_{(0.61)}$ photocatalyst under visible activation.

3.4. Photocatalytic activity and hydrogen generation using α-$MoO_{3(0.03)}$–$WO_{3(0.36)}$/$CdS_{(0.61)}$

In order to test the application possibility of the fabricated ternary photocatalyst, the photostability of the α-$MoO_{3(0.03)}$–$WO_{3(0.36)}$/$CdS_{(0.61)}$ photocatalyst was compared with pure CdS photocatalyst (Fig. 6a). Interestingly, the durability of the ternary nanocomposite showed about 19% loss of its photo-activity compared to 70% loss by CdS after the third cycle. Continuously, in comparison to 97% photoreduction by CdS alone, about 51.4% photoreduction occurred within 5 cycles using α-$MoO_{3(0.03)}$–$WO_{3(0.36)}$/$CdS_{(0.61)}$, resulting in its good photostability for photocatalytic applications in water environment. The higher photo-activity may come from the presence of the strong synergetic effect by ternary hybrid sample, that prevent the fastest photocorrosion to CdS by light and aqueous conditions.[34] Therefore, application of α-$MoO_{3(0.03)}$–$WO_{3(0.36)}$/$CdS_{(0.61)}$ for photo-remediation of an industrial wastewater containing 246.75 mg l^{-1} total organic carbon (TOC) was evaluated under visible and solar activation for 6 h. Fig. 6b shows that with time laps, the α-$MoO_{3(0.03)}$–$WO_{3(0.36)}$/$CdS_{(0.61)}$ photocatalyst exhibits relatively stable photocatalytic behavior with enhanced TOC reduction by 69.5% and 75% after 6 h under visible and solar irradiation, respectively. The enhanced solar photo-remediation performance was confirmed by an apparent first-order rate constant, K_{app}, (Fig. S7†),[35] which showed higher K_{app} by around 1.4 times for that under visible activation. It could be found also the photo-remediation of TOC was accompanied by the continued production of CO_2 gas, suggesting a complete removal of organic contaminants. Moreover, during the photocatalytic study, H_2 gas generation was noticed without any sign of deceleration (Fig. 6c). The photocatalytic hydrogen production rate was found around 6 and 8 μmol g^{-1} h^{-1} under visible and solar lights, respectively. Compared with literature focused on the photocatalytic hydrogen generation from organic contaminants;[36,37] obviously, in our case, the α-$MoO_{3(0.03)}$–$WO_{3(0.36)}$/$CdS_{(0.61)}$ has superior photocatalytic activities to achieve complete oxidation of TOC contaminants and reduce the donate electrons for H$^+$ ions for hydrogen generation under solar light.

The developed α-$MoO_{3(0.03)}$–$WO_{3(0.36)}$/$CdS_{(0.61)}$ nano-photocatalyst in this article triggered future interest and potential applications in the energy-related environmental issues compared with literature results of ternary photocatalyst counterparts and their composites. For example, Li et al.[30] reported that $Zn_{0.5}Cd_{0.5}S$ exhibits the maximum H_2-production rate of 7.42 mmol h^{-1} g^{-1} at 420 nm. In the work of Zhu et al.,[3] when 15% CdS coupled with TiO_2 (CdS15-TNTAs) gave the highest H_2 generation of 1.89 μmol h^{-1} cm^{-2} and 68.14% removal of Rh B dye after 5 h under visible irradiation. Shen et al.[20] reported that the MoO_3–CdS core–shell photocatalytic fabricated by sonochemical process has hydrogen production

rate of 5.25 mmol h^{-1} g^{-1} under the irradiation of visible-light. Further, non-oxide Ni-doped InN/GaZnON nanocomposite recorded H_2 evolution by rate of 2.23 μmol h^{-1} as reported by Hou et al.[38] The experimental results compared with literature data showed an improvement in the photocatalytic hydrogen performance of the developed ternary nanocomposite by the simple solid-state method. Therefore, in future research work, an optimization of hydrogen generation from different organic pollutants under different synthetic methodologies will be taken into account to enhance the hydrogen production rate.

3.5. Photocatalytic activity mechanism of the ternary hybrid photocatalyst

From the results in the present study, a tentative photo-excited charge transfer mechanism on α-$MoO_{3(0.03)}$–$WO_{3(0.36)}$/$CdS_{(0.61)}$ for TOC photo-remediation and H_2 generation is proposed and illustrated in Scheme 1. In this scheme, the heterojuncted ternary coupling leads to narrowing the charge transfer band gap energy by splitting the whole band edge into several sub-edges constrains, which is able to construct a Z-scheme system. Thereby, the Z-scheme prolonging the life time of photo-induced electrons–holes during the photocatalytic reactions. More importantly, the CB edge in heterojunction developed is just equal redox potential of H$^+$/H_2; whilst the VB edge is more than O_2/H_2O energy level (Scheme 1). As we know, the band gap of photocatalyst materials should be less than 3 eV to have a visible light response.[39] In solar spectrum, the solar light consists of ~5% ultraviolet and ~45–50% visible radiation, which able to excite the ternary photocatalyst (2.33 eV) components (α-MoO_3 3.05 eV, WO_3 2.72 eV and CdS 2.42 eV). However, both CdS and WO_3 were excited under visible radiation with an absorption band edge at 480–460 nm. On this basis, once heterojuncted α-$MoO_3(0.03)$–$WO_3(0.36)$/CdS(0.61) ternary photocatalyst is illuminated by solar light, two routes were supposed for the transfer of the photo-generated excited electrons, which is flow from the catalyst with a higher CB to the catalyst with a lower CB. For TOC photo-remediation, the photo-excited electrons of CdS were so lively to transfer from VB of CdS to CB of CdS. When photon with an equivalent or more energy hits the material surface, the generated electron in the CB of CdS (-0.422 eV) is transferred to the lower CB of α-MoO_3, and then electrons jump to produce high electrons concentration on the CB of WO_3. On the other hand, photo-generated holes' flow to the opposite direction and remain on the VB of the CdS (1.99 eV), which have the lowest positive potential. This processes was proceeded via the developed interfaces, in a favorable thermo-dynamically manner. In this case, the WO_3 and α-MoO_3 can act as electron transit station for both trapping electrons from the CdS, and thus more electron–hole pairs can be generated with increased lifetime as evidence by optical studies (cf. Section 3.2.2.). Electrons accumulated on the surface of α-MoO_3 and WO_3 react with adsorbed water and dissolved O_2 to generate reactive O_2^- species, while the photo-generated holes of CdS can react with OH$^-$ or H_2O forming hydroxyl radicals ($^{\bullet}OH$), and hydroperoxyl radicals ($^{\bullet}OOH$). Subsequently, the photo-generated strong oxidizing agents can oxidize and decompose

This journal is © The Royal Society of Chemistry 2017
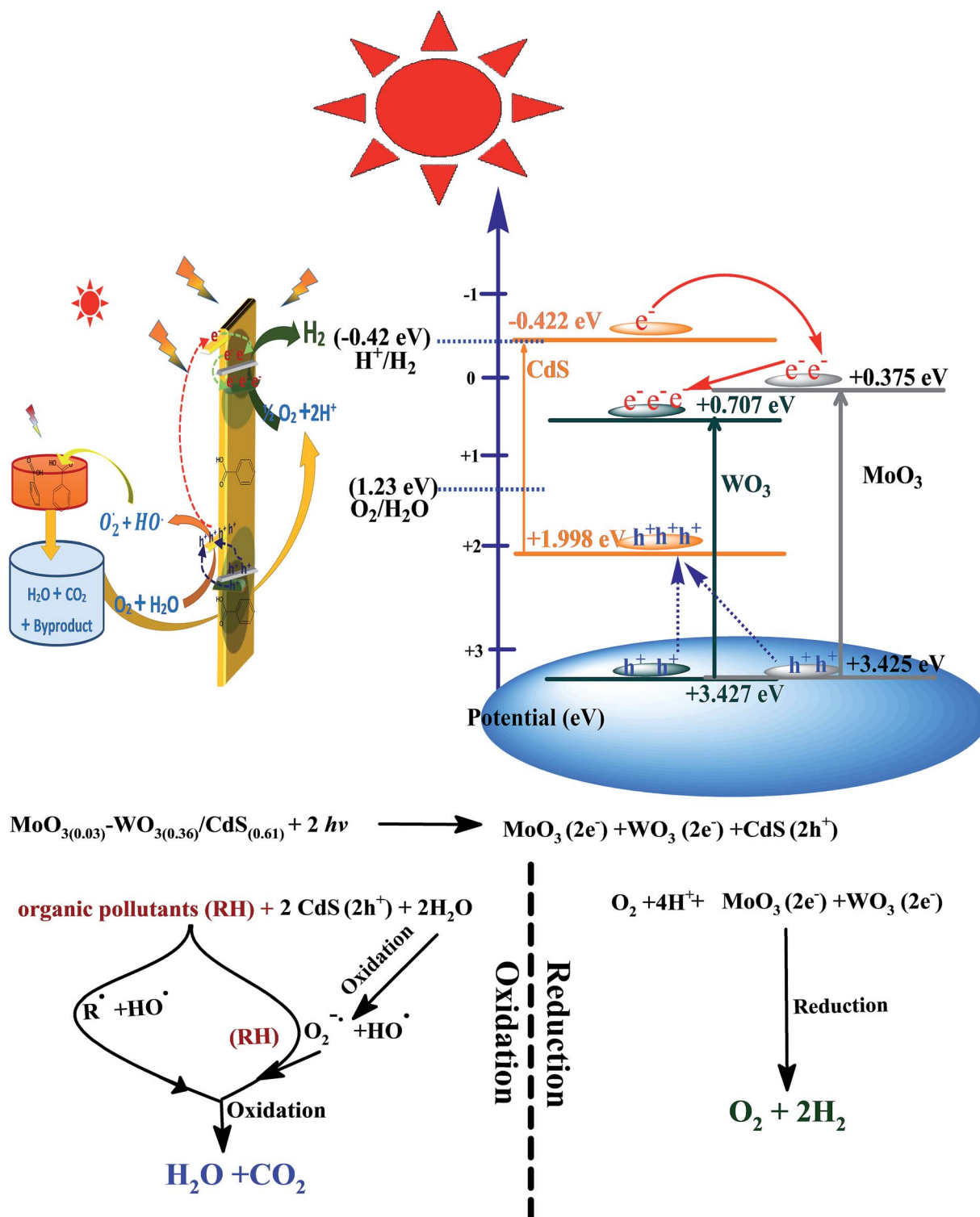
Scheme 1 Plausible photo-induced electron–hole pairs transfer and photo-degradation diagram over α-$MoO_{3(0.03)}$–$WO_{3(0.36)}$/$CdS_{(0.61)}$ ternary heterojunction solar harvester photocatalyst.

TOC organic pollutants to the inorganic molecules (CO_2 and H_2O). Similar photo-oxidation mechanisms have been reported elsewhere.[11,19,36,40,41] As for hydrogen production by the α-$MoO_{3(0.03)}$–$WO_{3(0.36)}$/$CdS_{(0.61)}$ photocatalytic system, the photo-excited electrons accumulated in the CB of the α-MoO_3 and

WO_3, electrons acceptor, can react with the adsorbed H^+ ions in solutions, at the active edges of WO_3 and then generate H_2 gas *via* reduction reaction mechanism.[34,42] Also, some photo-generated electrons in CdS nanowires can directly transferred to the CB of the α-MoO_3, and subsequently reduced H^+ to H_2

fuel gas. Furthermore, the interface quenching between the photo-generated electrons of α-MoO_3 and WO_3, and holes of CdS increase the stability of the developed α-$MoO_{3(0.03)}$–$WO_{3(0.36)}$/$CdS_{(0.61)}$ photocatalyst (*cf.* Section 3.4., Fig. 6a), which is also critical in determining the overall photocatalytic performance.

4. Conclusions

Herein, both SCD and BBD statistical optimal experimental designs were successfully used to fabricate a new α-$MoO_{3(0.03)}$–$WO_{3(0.36)}$/$CdS_{(0.61)}$ solar-harvester photocatalyst by a simple solid-state approach. It was noticed that the α-$MoO_{3(0.03)}$–$WO_{3(0.36)}$/$CdS_{(0.61)}$ developed as a single-phase crystal with 110 growth direction and a hierarchical heterojunction structure. Based on ODOE statistics data, three mathematical equations were developed and validated to simulate the relationship between the photocatalyst responses and combinatorial ratios of pure catalysts during synthesis and photocatalytic experimental conditions. The photodegradation efficiencies of the ternary photocatalyst increase with the appropriate combinatorial ratios of CdS and WO_3 accompanied by a decreased amount of α-MoO_3 catalyst. The reaction pH plays a most influential variable in the photodegradation rate (PC% 70.49%, *F*-value 8152.01, $p < 0.0001$) due to its antagonistic effect (*t*-test -90.29) on photo-excited reactive sites. More interestingly, the heterojuncted nanocomposite showed simultaneous photodegradation rate of 69.5% to 75% TOC pollutants and 6 to 8 μmol g^{-1} h^{-1} hydrogen generation from industrial wastewater under visible and solar lights, respectively. The new α-$MoO_{3(0.03)}$–$WO_{3(0.36)}$/$CdS_{(0.61)}$ exhibits good photocatalytic stability and durability even after 6 h and 5 cycles comparative to pure CdS catalyst. The promoted photocatalytic performance is due to the intimate interfaces interaction between CdS and α-MoO_3, and WO_3, and lower the optical band gap to $E_g = 2.33$ eV. The results presented in this work prove the effectiveness of ODOE strategy to design α-$MoO_{3(0.03)}$–$WO_{3(0.36)}$/$CdS_{(0.61)}$ solar harvester for efficient oxidation–reduction applications. Overall, the developed ternary heterojunction photocatalyst demonstrates a high potential feature for photo-remediation of total organic contaminants (TOC) and hydrogen production from wastewater under broad range of wavelengths. Future work on the potential use of the fabricated heterojuncted photocatalyst for solar-energy conversion will be investigated and optimized intensively.

References

1 V. V. Kumar, K. Gayathri and S. P. Anthony, *Mater. Res. Bull.*, 2016, **76**, 147–154.

2 A. A. Ismail, I. Abdelfattah, A. Helal, S. A. Al-Sayari, L. Robben and D. W. Bahnemann, *J. Hazard. Mater.*, 2016, **307**, 43–54.

3 Y. Zhu, Y. Wang, Z. Chen, L. Qin, L. Yang and L. Zhu, *Appl. Catal., A*, 2015, **498**, 159–166.

4 C. Sahoo and A. K. Gupta, *J. Hazard. Mater.*, 2012, **215–216**, 302–310.

5 B. Bajorowicz, A. Cybula, M. J. Winiarski, T. Klimczuk and A. Zaleska, *Molecules*, 2014, **19**, 15339–15360.

6 M. Khairy and W. Zakaria, *Egypt. J. Pet.*, 2014, **23**, 419–426.

7 J. Luo, X. Zhou, L. Ma and X. Xu, *J. Mol. Catal. A: Chem.*, 2015, **410**, 168–176.

8 M. V. Dozzi, S. Marzorati, M. Longhi, M. Coduri, L. Artiglia and E. Selli, *Appl. Catal., B*, 2016, **186**, 157–165.

9 T. Liu, B. Li, Y. Hao and Z. Yao, *Chem. Eng. J.*, 2014, **244**, 382–390.

10 N. Gupta and B. Pal, *J. Mol. Catal. A: Chem.*, 2014, **391**, 158–167.

11 H. Wang, W. Chen, J. Zhang, C. Huang and L. Mao, *Int. J. Hydrogen Energy*, 2015, **40**, 340–345.

12 C. W. Lai and S. Sreekantan, *Mater. Sci. Semicond. Process.*, 2013, **16**, 303–310.

13 P. Van Tong, N. D. Hoa, N. Van Duy, D. T. T. Le and N. Van Hieu, *Sens. Actuators, B*, 2016, **223**, 453–460.

14 J. Yang, J.-H. Zeng, S.-H. Yu, L. Yang, G. Zhou and Y.-T. Qian, *Chem. Mater.*, 2000, **12**, 3259–3263.

15 Y. Li, X. Li, C. Yang and Y. Li, *J. Mater. Chem.*, 2003, **13**, 2641–2648.

16 H. Hassan, T. Zaki, S. Mikhail, A. Kandil and A. Farag, *ISRN Nanomater.*, 2012, 909647.

17 T. Zaki, K. I. Kabel and H. Hassan, *Ceram. Int.*, 2012, **38**, 4861–4866.

18 O. W. Gooding, *Curr. Opin. Chem. Biol.*, 2004, **8**, 297–304.

19 X. Liu, Y. Yan, Z. Da, W. Shi, C. Ma, P. Lv, Y. Tang, G. Yao, Y. Wu, P. Huo and Y. Yan, *Chem. Eng. J.*, 2014, **241**, 243–250.

20 Z. Shen, G. Chen, G. Yu, Q. Wang, C. Zhou, L. Hao, Y. Li, L. He and R. Mu, *J. Mater. Chem.*, 2012, **22**, 19646–19651.

21 K. Huang, Q. Pan, F. Yang, S. Ni, X. Wei and D. He, *J. Phys. D: Appl. Phys.*, 2008, **41**, 155417.

22 T. Siciliano, A. Tepore, E. Filippo, G. Micocci and M. Tepore, *Mater. Chem. Phys.*, 2009, **114**, 687–691.

23 D. Chen, M. Liu, L. Yin, T. Li, Z. Yang, X. Li, B. Fan, H. Wang, R. Zhang and Z. Li, *J. Mater. Chem.*, 2011, **21**, 9332–9342.

24 P. Kumar, N. Saxena, R. Chandra, V. Gupta, A. Agarwal and D. Kanjilal, *Nanoscale Res. Lett.*, 2012, **7**, 1–7.

25 L. Xu, M.-L. Yin and S. F. Liu, *Sci. Rep.*, 2014, **4**, 6745–6752.

26 D. Vernardou, H. Drosos, E. Spanakis, E. Koudoumas, C. Savvakis and N. Katsarakis, *J. Mater. Chem.*, 2011, **21**, 513–517.

27 F. Barzegar, A. Bello, D. Y. Momodu, J. K. Dangbegnon, F. Taghizadeh, M. J. Madito, T. M. Masikhwa and N. Manyala, *RSC Adv.*, 2015, **5**, 37462–37468.

28 H. Cheng, J. Wang, Y. Zhao and X. Han, *RSC Adv.*, 2014, **4**, 47031–47038.

29 F. Amano, K. Nogami, M. Tanaka and B. Ohtani, *Langmuir*, 2010, **26**, 7174–7180.

30 Q. Li, H. Meng, P. Zhou, Y. Zheng, J. Wang, J. Yu and J. Gong, *ACS Catal.*, 2013, **3**, 882–889.

31 E. Hong, D. Kim and J. H. Kim, *J. Ind. Eng. Chem.*, 2014, **20**, 3869–3874.

32 N. Li, Y. Li, W. Li, S. Ji and P. Jin, *J. Phys. Chem. C*, 2016, **120**, 3341–3349.

33 H. Li, Y. Zhou, L. Chen, W. Luo, Q. Xu, X. Wang, M. Xiao and Z. Zou, *Nanoscale*, 2013, **5**, 11933–11939.

34 Y. Zhu, Y. Wang, Z. Chen, L. Qin, L. Yang, L. Zhu, P. Tang, T. Gao, Y. Huang, Z. Sha and G. Tang, *Appl. Catal., A*, 2015, **498**, 159–166.

35 H. J. Lee, J. H. Kim, S. S. Park, S. S. Hong and G. D. Lee, *J. Ind. Eng. Chem.*, 2015, **25**, 199–206.

36 X. Wang and X. Y. Li, *Mater. Sci. Eng., B*, 2014, **181**, 86–92.

37 E. Su, B. Huang, C. Liu and M. Wey, *Renewable Energy*, 2015, **75**, 266–271.

38 X. Hou, S. Jiang, Y. Li, J. Xiao and Y. Li, *Int. J. Hydrogen Energy*, 2015, **40**, 15448–15453.

39 T. Jafari, E. Moharreri, A. Amin, R. Miao, W. Song and S. Suib, *Molecules*, 2016, **21**, 900–929.

40 S. Bai, H. Liu, J. Sun, Y. Tian, S. Chen, J. Song, R. Luo, D. Li, A. Chen and C. C. Liu, *Appl. Surf. Sci.*, 2015, **338**, 61–68.

41 T. Choi, J.-S. Kim and J. H. Kim, *Adv. Powder Technol.*, 2016, 1–7.

42 W. K. Jo and N. C. Sagaya Selvam, *Appl. Catal., A*, 2016, **525**, 9–22.